ACS APPLIED MATERIALS & INTERFACES

Research Article

www.acsami.org

Electrostatic Self-Assembly of $BiVO_4$–Reduced Graphene Oxide Nanocomposites for Highly Efficient Visible Light Photocatalytic Activities

Yinzhou Wang,[†] Wei Wang,[†] Hongying Mao,[‡] Yunhao Lu,[†] Jianguo Lu,[†] Jingyun Huang,[†] Zhizhen Ye,[†] and Bin Lu*[,†]

[†]State Key Laboratory of Silicon Materials, Department of Materials Science and Engineering, Zhejiang University, Hangzhou 310027, People's Republic of China

[‡]Department of Physics, Hangzhou Normal University, Hangzhou 310036, People's Republic of China

Supporting Information

ABSTRACT: It is commonly considered that the morphology and interface of semiconductor–reduced graphene oxide (rGO) composite photocatalysts play a crucial role in determining their photocatalyzing performance. Herein, we report on the design and synthesis of $BiVO_4$–rGO nanocomposites with efficient interfacial contact by self-assembly of positively charged amorphous $BiVO_4$ powders with negatively charged graphene oxide (GO), followed by a one-step GO reduction and $BiVO_4$ crystallization via hydrothermal treatment. The as-prepared $BiVO_4$–rGO nanocomposites exhibit high visible light photocatalytic efficiency for the degradation of model dyes, and are significantly superior to bare crystalline $BiVO_4$ and $BiVO_4$–rGO–U that is hydrothermally synthesized using the mixture of GO nanosheets and $BiVO_4$ powders without modification of surface charge. Using multiple characterization techniques, we found that the enhanced photocatalytic performance of $BiVO_4$–rGO arises from the synergistic effects between the microscopic crystal structure of $BiVO_4$ with smaller particle size and more sufficient interfacial interaction between $BiVO_4$ and graphene sheets, leading to increased photocatalytic reaction sites, extended photoresponding range, enhanced photogenerated charge separation, and transportation efficiency. This work may provide a rational and convenient strategy to construct highly efficient semiconductor–rGO nanocomposite photocatalysts with well-contacted interface toward environmental purification and solar energy conversion.

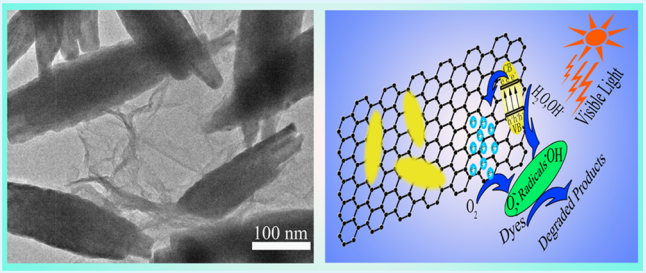

KEYWORDS: *rGO, self-assembly, surface charge modification, interfacial interaction, photocatalysis*

INTRODUCTION

Environmental pollution and energy shortage are becoming the topic issues in the sustainable development of human society. Photocatalytic reaction, as a potential solution to the energy production and environmental pollutant control, has drawn much attention. Various semiconductor photocatalysts, such as TiO_2, WO_3, ZnO, CdS, and Ag_3PO_4, have been investigated for photocatalytic degradation of pollutants and hydrogen generation from water splitting.[1−5] Most of them suffer from wide bandgap, photocorrosion, and low separation efficiency of electron–hole pairs.[6−10] To address these problems, many efforts, such as doping, composites, noble metal loading, and heterojunction fabrication have been made.[11−14] Among these, constructing graphene-based nanocomposites is a promising approach to obtain high performance photocatalysts. To date, a variety of rGO-based semiconductor (e.g., TiO_2, CdS, ZnO, and Ag_3PO_4) composite photocatalysts have been reported.[15−18] Typically, these composite photocatalysts were synthesized by preparing semiconductor powders and graphene oxide (GO) colloidal solution as precursors, followed by the reduction of GO to rGO via hydrothermal reduction, hydrazine reduction, or UV-irradiation reduction method.[19,20] The widely accepted mechanism for photocatalytic performance enhancement is that chemical bonding between rGO and semiconductor could accelerate the transfer of photogenerated electrons in semiconductor to rGO, thus suppressing the recombination of photogenerated carriers effectively.[21,22] By tuning the interaction strength between semiconductor and rGO, it is possible to change the photocatalytic activities of these composite photocatalysts.[19]

Bismuth vanadate ($BiVO_4$), as one of the most promising visible-light driven photocatalysts, has been widely studied for photodegradation of pollutant and solar energy conversion.[23−26] The relatively narrow band gap (2.4 eV) of $BiVO_4$ can provide effective utilization of visible light.[27] More critically, as compared to other semiconductors, it has lighter effective masses of electrons and holes, which provides advantages to improve the separation efficiency of photogenerated

Received: May 3, 2014
Accepted: July 10, 2014
Published: July 10, 2014

charges.[24,28] However, $BiVO_4$ is insoluble in water, and amorphous $BiVO_4$ nanoparticles tend to aggregate rapidly after the mixing of hydrothermal precursors, which makes it hard to obtain $BiVO_4$ crystals with small particle size and uniform morphology by traditional solution-phase methods.[29] Considering the small specific surface area of traditionally synthesized $BiVO_4$, its photocatalytic performance is usually low. To address this problem, significant efforts have been made to obtain uniform monoclinic $BiVO_4$ nanocrystals with high activities.[30] With the use of a template, Eda et al. synthesized monoclinic sheelite $BiVO_4$ nanorods by using polyethylene glycol.[31] Kudo et al. synthesized $BiVO_4$ nanofibrous arrays via a hydrothermal route under the assistance of a cationic surfactant, cetyltrimethylammonium bromide (CTAB).[32] In addition, the synthesis of loosely packed monoclinic $BiVO_4$ nanoellipsoids by introduction of oleic acid as surfactant is also reported.[33] Nevertheless, organic templates or surfactants are usually expensive and even toxic, and would hardly be removed completely by postsynthetic processes. The residues could do harm to photocatalytic activities of the synthesized photocatalysts. That is, preparation of uniform, small-sized $BiVO_4$ without any organic templates or surfactants remains challenging. To improve the photocatalytic activities of bare $BiVO_4$, fabrication of $BiVO_4$–rGO composites was proposed.[34−36] However, a simple mixing of semiconductor powders and GO colloidal solution followed by a hydrothermal treatment can hardly ensure strong and sufficient interaction between semiconductor particles and rGO sheets, limiting the enhancement of their photocatalytic activities.[37]

In this Article, we report on the modification and photocatalytic performance improvement of $BiVO_4$ (am–$BiVO_4$) powders via a simple surface charge method with the aid of (3-aminopropyl)triethoxysilane (APTES). The positively charged am–$BiVO_4$ powders were first coupled with negatively charged GO by electrostatic attractive interaction, followed by crystallization of $BiVO_4$ and reduction of GO to rGO via a simple hydrothermal reduction method. With this method, not only efficient interfacial interaction between $BiVO_4$ nanoparticles and graphene nanosheets, but also small particle size of $BiVO_4$ was achieved. The small-sized particles and strong interfacial interaction contribute to increased specific reaction sites, extended photoresponding range, and enhanced photogenerated charges transportation and separation efficiency, resulting in an improvement of the photocatalytic activities. The $BiVO_4$–rGO nanocomposites exhibit much higher visible light photocatalytic activities for the degradation of model dyes than that of bare $BiVO_4$ and $BiVO_4$–rGO–U with large particle size, which is simply hydrothermally synthesized by mixing unmodified $BiVO_4$ powders with GO. This work may provide new insights into the fabrication of semiconductor–rGO nanocomposite photocatalysts via electrostatic self-assembly.

EXPERIMENTAL DETAILS

The procedures for synthesizing $BiVO_4$–rGO are shown in Scheme 1. It consists of three main steps: surface charge modification on am–$BiVO_4$ powders, synthesis of GO nanosheets, crystallization of $BiVO_4$ particles, and reduction of GO simultaneously by a hydrothermal method.

Preparation of APTES-Modified am–$BiVO_4$ Powder. In a typical synthesis, $Bi(NO_3)_3{\cdot}5H_2O$ and NH_4VO_3 at a molar ratio of 1:1 were dissolved in HNO_3 (50 mL, 2 M) and NaOH (50 mL, 2 M) respectively. A uniform orange suspension was formed by mixing these solutions under continuous stirring. After 1 h of stirring at room temperature, am–$BiVO_4$ powder was collected with centrifugation,

Scheme 1. Schematic Illustration for the Synthesis of $BiVO_4$–rGO Nanocomposite Photocatalysts via Electrostatic Self-Assembly Accompanied by a Hydrothermal Reduction Process

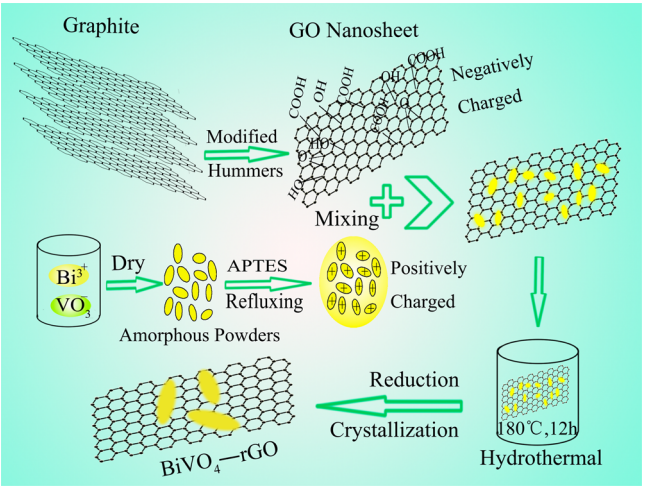

washed with deionized water, and dried at 333 K in air. The am–$BiVO_4$ powders were functionalized by APTES. That is, 2.0 g of am–$BiVO_4$ powders was first dispersed in 400 mL of ethanol by ultrasonication for 30 min. Next, 0.5 mL of APTES was added, and am–$BiVO_4$ powders were treated in refluxing ethanol solution containing APTES at 353 K for 4 h. The product was collected and washed sufficiently with ethanol by centrifugation, followed by drying at 333 K in air.

Synthesis of GO Nanosheets. GO nanosheets were synthesized from graphite powder according to the modified Hummers method.[15,38] The details of the typical process are presented in the Supporting Information.

Fabrication of $BiVO_4$–rGO Nanocomposite Photocatalysts. $BiVO_4$–rGO nanocomposites were fabricated via the standard hydrothermal method. In brief, 0.5 g of APTES-modified am–$BiVO_4$ powder was dispersed in 150 mL of deionized water by ultrasonication for 10 min; then 25 mL of GO suspension (1 mg/mL) was added into the above $BiVO_4$ suspension under vigorous stirring at pH = 6, acquiring the weight ratio of GO to $BiVO_4$ at 0.05:1. After being stirred for 2 h, a homogeneous suspension formed. The suspension was then transferred to a Teflon-sealed autoclave and maintained at 453 K for 12 h to simultaneously achieve the crystallization of $BiVO_4$ particles and the reduction of GO to rGO. For comparison, $BiVO_4$–rGO–U was synthesized in the same way using unmodified am–$BiVO_4$ powders, instead of the modified ones.

Characterization and Measurements. Powder XRD characterization was carried out with a Shimadzu XRD-6000 diffractometer with Cu Kα radiation (λ = 0.15418 nm). Morphologies and particle sizes of samples were examined by SEM (Hitachi S-4800) and TEM (Philips Tecnai F20) operated at 200 kV. Energy dispersive spectroscopy (EDS) was also taken with S-4800 SEM. X-ray photoelectron spectra (XPS) were measured on an Escalab 250Xi system (Thermo Scientific) using Mg Kα radiation of 1253.6 eV. Raman spectra were performed using a Raman spectrometer (LabRamHRUV), excited with the 514 nm line of argon-ion laser at an incident power of 10 mW. The Brunauer–Emmett–Teller (BET) specific surface area of the samples was analyzed by nitrogen (N_2) adsorption–desorption in a Quantacrome Autosorb-1-C instrument. Photoluminescence (PL) spectra were acquired on an Edinburgh Instruments FLS920 fluorescence spectrometer, equipped with Xe 900 lamp and 392 nm filters. UV–vis diffuse reflectance spectra (DRS) were recorded in the range from 350 to 800 nm with a Shimadzu UV-3600 spectrophotometer equipped with an integrating sphere attachment.

Zeta potential measurements were performed using the Zetasizer3000HSA (Malvern Instruments). Briefly, 5 mg of the sample was

dispersed in 50 mL of deionized water by ultrasonication at room temperature. Also, pH was adjusted to 6 before the measurements.

A CHI660B workstation (Chenhua Instrument) was employed for electrochemical impedance spectroscopy (EIS) measurements. EIS measurements were carried out in 0.2 M aqueous Na_2SO_4 solution without any additive, using a three-electrode system. Platinum foil electrodes and Ag/AgCl electrodes were used as counter electrodes and reference electrodes, respectively. For the EIS measurements, powder samples were fabricated as working electrodes with reported methods.[15,34] First, 3 mg of sample powder was dispersed in 0.5 mL of *N*,*N*-dimethylformamide (DMF) by ultrasonication. The obtained slurry was then spread on the conductive indium tin oxides glass substrates, acquiring a ca. 1 cm^2 active area with aids of adhesive tapes and sealants. Finally, the resultant working electrodes were dried at 333 K overnight. EIS was recorded at room temperature, with AC voltage amplitude of 5 mV, and a frequency range from 1 MHz to 0.1 Hz at 0 V.

Photocatalytic Reactions. Photocatalytic experiments were performed with methyl blue (MB) and rhodamine B (RhB) under ambient conditions. A 300 W Xe arc lamp (PLS-SXE 300C) equipped with a filter to cut off light of wavelength below 400 nm was used as irradiation source. Aqueous solutions of dyes and photocatalysts placed in cylindrical quartz vessel were exposed to the visible light irradiation under ambient conditions and stirring. In detail, 0.1 g of as-prepared photocatalyst was added into 100 mL of MB (10 mg/L) and RhB (10 mg/L) aqueous solution, respectively. The mixture was then ultrasonicated for 10 min and stirred for 30 min in the dark to reach adsorption−desorption equilibrium between the samples and the reactant prior to the illumination. Next, Xe arc lamp was turned on to start the photocatalytic reaction. Since then, 5 mL of mixture solution was withdrawn and centrifuged to remove the catalyst at given time intervals. Absorption spectra of the centrifuged solution were recorded with the UV-3600 spectrophotometer. For comparison, photodegradation experiments of MB and RhB were also carried out without addition of photocatalysts under the same conditions. The degree of photodegradation was calculated from the absorbance of dyes at their specific wavelength according to the literature.[39,40]

RESULTS AND DISCUSSION

Crystal Phase and Composition. Figure 1 shows XRD patterns of bare $BiVO_4$, $BiVO_4$−rGO−U, and $BiVO_4$−rGO. It

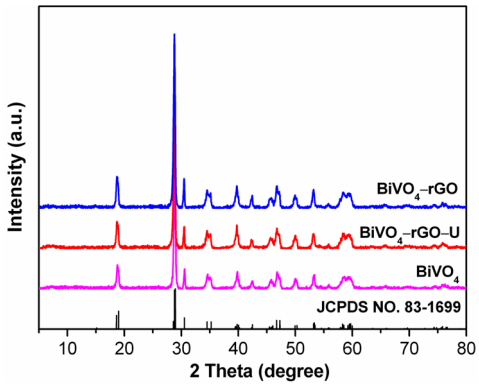

Figure 1. XRD patterns of bare $BiVO_4$, $BiVO_4$−rGO−U, and $BiVO_4$−rGO nanocomposites.

can be seen that the XRD pattern of bare $BiVO_4$ could be indexed to the well-crystallized monoclinic $BiVO_4$ phase (JCPDS no. 83-1699) as marked. $BiVO_4$−rGO−U and $BiVO_4$−rGO nanocomposites show coincident XRD patterns to bare $BiVO_4$, without observation of any diffraction peaks from rGO due to the relatively limited rGO amount in the nanocomposites.[15,37]

The typical Raman spectra of these samples are presented in Figure 2a, showing peaks at 820, 707, 366, 323, and 210 cm^{-1}

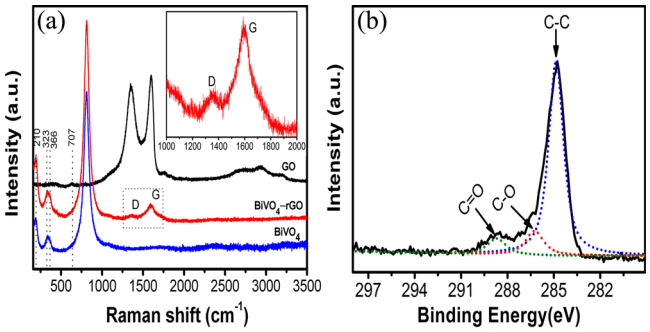

Figure 2. Raman spectra of bare $BiVO_4$, GO, and $BiVO_4$−rGO (a), and high-resolution core level XPS spectrum of C 1s (b) of the $BiVO_4$−rGO nanocomposites. The inset of (a) is an enlarged view of D/G-bands of $BiVO_4$−rGO.

for bare $BiVO_4$, in agreement with previous reports.[41] The dominated peak at 820 cm^{-1} and inconspicuous peak at 707 cm^{-1} are assigned to the symmetric and antisymmetric V−O stretching modes, respectively. Peaks centered at 366 and 323 cm^{-1} are attributed to the typical symmetric and antisymmetric bending modes of the vanadate anion, respectively, and are merged into an integrated broad peak due to the adjacent values. The peak at 210 cm^{-1} is an external mode. GO exhibits Raman shifts at 1599 and 1363 cm^{-1}, corresponding to the G- and D-bands, respectively. As for the $BiVO_4$−rGO nanocomposites, besides the distinctive peaks assigned to $BiVO_4$, the G- and D-bands of rGO are located at 1590 and 1351 cm^{-1}, respectively, indicating shifts toward lower wavenumber as compared to GO. This trend is attributed to the recovery of hexagonal network of carbon atoms with defects during the reduction process.[42] Because the D/G ratio can be used to evaluate the average size of the sp^2 domains inversely,[43] the diminished D/G ratio of $BiVO_4$−rGO implies that the reduction of GO increased the average size of the graphene domains. To further clarify the composition of the $BiVO_4$−rGO nanocomposites, XPS measurements are performed as shown in Supporting Information Figure S1, suggesting the definite combination of $BiVO_4$ with rGO in the sample. In the high-resolution spectrum of C 1s (Figure 2b), carbons in the form of sp^2 bonds (284.6 eV) are dominated, and oxygen-containing functional groups can also be observed at 286.6 eV (C−O, epoxy, and hydroxyl) and 288.9 eV (C═O, carboxyl). The fairly low peak intensity for oxygenated functional groups indicates efficient removal of oxygen-containing functional groups during the hydrothermal process.

Morphology. The morphologies of the as-prepared samples are investigated by SEM and TEM. As shown in Figure 3a and b, for both the bare $BiVO_4$ and the $BiVO_4$−rGO−U, the $BiVO_4$ particles exhibit well-defined pillar-like morphologies, with an average size of 1−2 μm. One can find that the pillar-like aggregates are composed of many nanoparticles and their surfaces are rather rough. As for the $BiVO_4$−rGO−U, rGO nanosheets can be found wrapping the pillar-like $BiVO_4$ particles. Because of the relatively large particle size and rough morphology of aggregated $BiVO_4$ particles, it would be hardly possible to form sufficient interfacial contact between $BiVO_4$ particles and rGO nanosheets. Fortunately, the situation is quite different for that of $BiVO_4$−rGO sample. As shown in

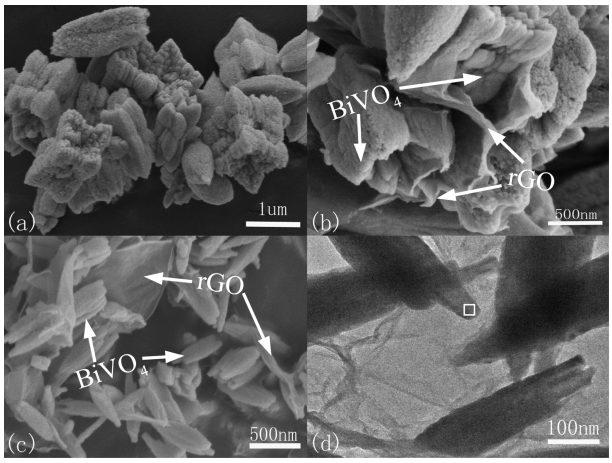

Figure 3. Typical SEM images of $BiVO_4$ (a), $BiVO_4$–rGO–U (b), $BiVO_4$–rGO (c), and TEM image of $BiVO_4$–rGO (d).

Figure 3c and d, the $BiVO_4$ nanoparticles exhibit spindle-like morphologies, with a mean length of ~500 nm and an average width of ~100 nm, significantly smaller than that observed in bare $BiVO_4$ and $BiVO_4$–rGO–U. The spindle-like $BiVO_4$ nanoparticles are densely covered with rGO nanosheets (Figure 3c), implying the possibility of sufficient contact and efficient interfacial interaction between $BiVO_4$ and rGO.

Nitrogen adsorption–desorption isotherms (Figure 4) for these three samples are given for further investigation of their

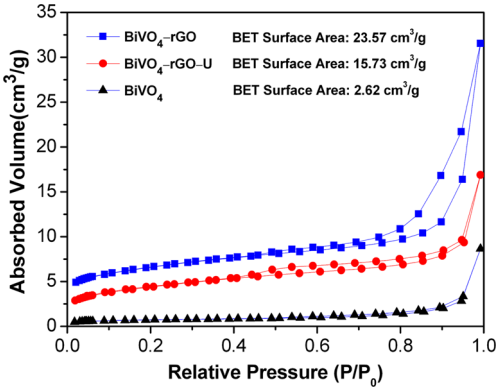

Figure 4. BET adsorption–desorption isotherm of bare $BiVO_4$, $BiVO_4$–rGO, and $BiVO_4$–rGO–U nanocomposites.

morphologies. All of them exhibit the type-IV isotherm with a typical H3 hysteresis loop characteristic of mesoporous solids. The specific BET surface areas are 23.57, 15.73, and 2.62 cm^3/g for $BiVO_4$–rGO, $BiVO_4$–rGO–U, and bare $BiVO_4$, respectively. EDS analysis (Supporting Information Figure S2) of the $BiVO_4$–rGO sample shows the presence of four elements in the nanocomposites: Bi, V, O, and C, confirming the incorporation of rGO into the final products. TEM image (Figure 3d) clearly reveals that the $BiVO_4$ nanoparticles are interconnected with rGO nanosheets. HRTEM image (Supporting Information Figure S3) taken from the square area indicated in Figure 3d shows lattice fringe spacing of 0.584 and 0.468 nm, matching well with (002) and (011) lattice planes of monoclinic $BiVO_4$.

Formation Mechanism. The only difference in synthesis processes between $BiVO_4$–rGO and $BiVO_4$–rGO–U is the surface charge modification procedure on am–$BiVO_4$ prior to the mixing of am–$BiVO_4$ powders and GO colloidal as hydrothermal precursors. It is thus believed that surface charge modification plays an important role in the construction of efficient $BiVO_4$–rGO nanocomposite photocatalyst. A rational explanation for the morphology difference is that electrostatic force may effectively inhibit the aggregation of $BiVO_4$ nanoparticles. On one hand, the electrostatic attraction drives the self-assembly of positively charged $BiVO_4$ nanoparticles and negatively charged GO nanosheets, moving most of the am–$BiVO_4$ particles anchored on GO nanosheets. On the other hand, the mutual electrostatic repulsion of positively charged $BiVO_4$ nanoparticles impedes the aggregation of am–$BiVO_4$. Afterward, during the hydrothermal crystallization process, am–$BiVO_4$ nanoparticles crystallized and constructed spindle-like $BiVO_4$ ellipsoids through oriented aggregation on the rGO nanosheet templates rather than formation of micrometer-sized pillar-like particles. The structural features with small-sized $BiVO_4$ and sufficient interfacial contact between $BiVO_4$ nanoparticles and rGO nanosheets will help to provide increased photocatalytic reaction sites, and enhanced photogenerated charges transportation and separation efficiency. Similar influences of surface charge modification could also be found in other reports.[37,44–46]

The different interfacial contact of $BiVO_4$ particles with rGO nanosheets between $BiVO_4$–rGO and $BiVO_4$–rGO–U is further evidenced by photographs (Figure 5) taken before

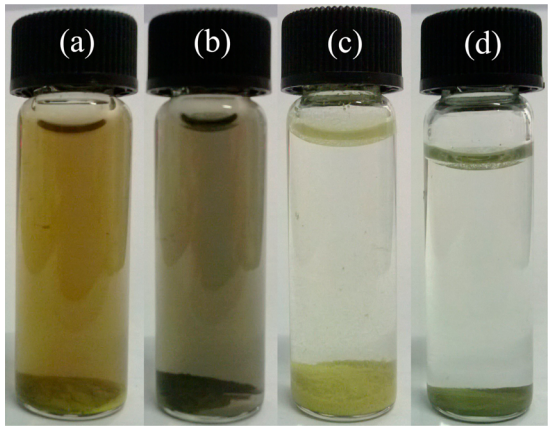

Figure 5. Photographs of $BiVO_4$–rGO–U before (a) and after (b) hydrothermal process, and $BiVO_4$–rGO before (c) and after (d) hydrothermal process.

and after hydrothermal process. For the $BiVO_4$–rGO–U synthesized with unmodified am–$BiVO_4$, the upper opaque suspension turned from brown to dark after hydrothermal treatment, implying relatively weak interaction between rGO and $BiVO_4$. The solution for $BiVO_4$–rGO obtained from electrostatic self-assembly is clear and clarified with most solutes settled at the bottom.

The enhanced interfacial interaction between rGO and $BiVO_4$ that resulted from surface charge modification can be reasonably explained by zeta potential analysis (Figure 6). At pH = 6, GO and am–$BiVO_4$ aqueous dispersions exhibit obvious negatively charged surface with a zeta potential value of −56.9 and −31.4 mV, respectively. However, the zeta potential value of APTES-modified am–$BiVO_4$ becomes +4 mV under the same test conditions. That is, APTES treatment has changed the polarity of surface charges of $BiVO_4$. When APTES-modified am–$BiVO_4$ powders and GO colloidal are

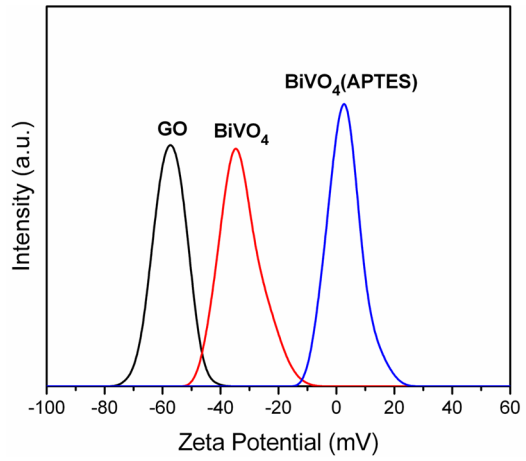

Figure 6. Zeta potential of GO, amorphous $BiVO_4$, and amorphous $BiVO_4$ treated with (3-aminopropyl) triethoxysilane (APTES).

mixed in aqueous solution, electrostatic attraction makes them self-assemble into well-contacted $BiVO_4$–GO nanocomposites. Another merit of the adequate interfacial interaction is that substantial aggregates of $BiVO_4$ particles would not occur during the following hydrothermal crystallization process. Thus, $BiVO_4$–rGO nanocomposites with sufficient interfacial contact and small particle sized $BiVO_4$ are constructed via a simple electrostatic self-assembly. In contrast, as for the $BiVO_4$–rGO–U, due to mutual electrostatic repulsion between the negatively charged precursors, the interfacial interaction of $BiVO_4$ and GO/rGO is insufficient with additional GO/rGO dispersed in the solution, resulting in the observed suspension as shown in Figure 5a,b.

Photocatalytic Degradation. The photocatalytic performance of the as-prepared bare $BiVO_4$, $BiVO_4$–rGO–U, and $BiVO_4$–rGO is evaluated by the degradation of model dyes (MB and RhB). The degree of dye photodegradation is obtained by calculating the change of concentration (C/C_0) from the variation of absorbance at the specific wavelength of model dyes. The photodegradation rate is calculated by the formula: photodegradation rate = $(C_0 - C)/C_0$, where C_0 and C are the concentrations of primal and photodecomposed dyes, respectively. According to the Langmuir–Hinshelwood first-order reaction kinetics behavior, the pseudo-first-order rate constants (k) for different photocatalysts can be calculated by the formula: $\ln(C_0/C) = kt$, where k and t represent rate constant and time, respectively.[47] The rate constants (k) for different photocatalysts can be obtained by plotting $\ln(C_0/C)$ versus t, acquiring the k values from slopes of the graphs.

Figures 7 and 8 display the photodegradation rates of MB and RhB, respectively. For comparison, results of blank photolysis experiments for MB and RhB are also provided (Supporting Information Figure S4). One can see that the removal efficiency of dyes is negligible when no photocatalysts are added. For $BiVO_4$–rGO, the photodegradation rate of MB reaches 94.1% after irradiation for 30 min. However, photodegradation rates are just 34.3% and 24.1% after the same time of irradiation when the photocatalysts are replaced by $BiVO_4$–rGO–U and bare $BiVO_4$, respectively. After another 30 min, the photodegradation rate reaches 51.5% ($BiVO_4$–rGO–U) and 50.3% ($BiVO_4$). The corresponding pseudo-first-order kinetic plots are shown in the inset of Figure 7. The rate constants for $BiVO_4$–rGO, $BiVO_4$–rGO–U, and bare $BiVO_4$ are 8.45×10^{-2}, 1.27×10^{-2}, and 1.06×10^{-2} min^{-1},

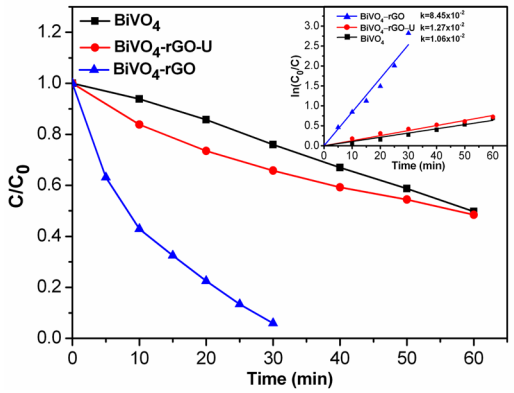

Figure 7. Photodegradation of methylene blue (MB) under visible light (λ > 400 nm) over the bare $BiVO_4$, $BiVO_4$–rGO–U, and $BiVO_4$–rGO photocatalysts.

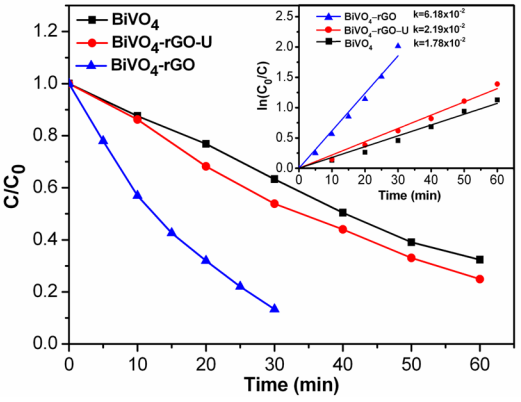

Figure 8. Photodegradation of rhodamine B (RhB) under visible light (λ > 400 nm) over the bare $BiVO_4$, $BiVO_4$–rGO–U, and $BiVO_4$–rGO photocatalysts.

respectively, following the sequence $BiVO_4$–rGO > $BiVO_4$–rGO–U > bare $BiVO_4$. Similar results have occurred in regard to the degradation of RhB (Figure 8), accompanied by the highest photocatalytic activity of $BiVO_4$–rGO nanocomposites. As expected, RhB is barely degraded at all in the absence of photocatalysts due to its high stability under visible light irradiation. The photodegradation rate is remarkably accelerated with $BiVO_4$–rGO nanocomposites (rate constant $k = 6.18 \times 10^{-2}$ min^{-1}), significantly higher than that of $BiVO_4$–rGO–U ($k = 2.19 \times 10^{-2}$ min^{-1}) and bare $BiVO_4$ powders ($k = 1.78 \times 10^{-2}$ min^{-1}).

On the basis of the above experimental results, it is inferred that the $BiVO_4$–rGO nanocomposites with specific structural features and intimate interfacial contact between $BiVO_4$ and rGO will give rise to remarkable photocatalytic performance enhancement.

Mechanism for Photocatalytic Activity Enhancement. To understand the origins and get deep insights into the enhanced photocatalytic performance of $BiVO_4$–rGO nanocomposites, multiple investigations have been carried out. The first effect one can reasonably imagine is that the enhancement in photoactivity was caused by morphology change. The small-particle-sized $BiVO_4$ with less aggregation (providing larger surface-to-bulk ratio) could not only help to significantly increase the reaction area for pollutants, but also effectively inhibit the electron–hole recombination between $BiVO_4$

particles, which would be beneficial to photocatalytic properties.

Another synergistic effect that contributed to the improved photocatalytic activity of $BiVO_4$–rGO may come from the extended photoresponding range. UV–vis DRS spectra of $BiVO_4$ and $BiVO_4$–rGO are shown in Figure 9. It can be seen

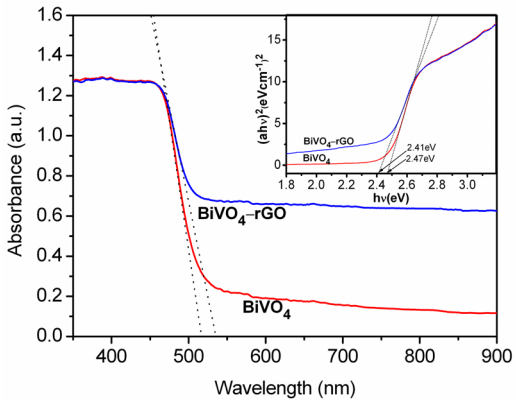

Figure 9. UV–vis diffuse reflectance spectra of bare $BiVO_4$ and $BiVO_4$–rGO nanocomposites. The inset is plots of $(\alpha h\nu)^2$ versus photon energy $(h\nu)$ of the corresponding samples.

that the band gap absorption edges of the bare $BiVO_4$ and $BiVO_4$–rGO nanocomposites are 516 and 535 nm, respectively. The band gap energy can be estimated from the DRS data.[48,49] As shown in the inset of Figure 9, the band gaps of bare $BiVO_4$ and $BiVO_4$–rGO nanocomposites are estimated to be 2.47 and 2.41 eV, respectively. The inconspicuous band gap narrowing should be attributed to chemical bonding between $BiVO_4$ and rGO, that is, probably the formation of Bi–C bond in $BiVO_4$–rGO. During the hydrothermal treatment of $BiVO_4$-GO, Bi atoms in the amorphous phase should interact more actively with GO sheets. In addition, oxygen-containing functional groups on the surface of GO vanish during the hydrothermal process, leaving unpaired π electrons on rGO sheets, which could easily bond with more Bi atoms on the surface of $BiVO_4$ during the phase transformation process. As a result, a surface doping-like behavior should appear, leading to the energy level change of conduction band, as that suggested previously in TiO_2–rGO nanocomposites.[15,46] The light absorption range extension could achieve a more efficient utilization of the solar spectrum and an enhancement of the photocatalytic activity. Moreover, the addition of rGO results in a remarkable enhancement of background absorption in the visible light region, which might be attributed to the reintroduction of blackbody properties of rGO, indicating sufficient reduction of GO to rGO during hydrothermal reduction process.[50]

Finally, the eminently improved visible light photoactivity of $BiVO_4$–rGO nanocomposites could be mainly ascribed to the intimate interfacial contact of $BiVO_4$ and rGO. To present evidence to support this viewpoint, EIS Nyquist analysis has been conducted at a frequency range from 0.1 Hz to 1 MHz. The high-frequency arc in EIS corresponds to the charge transfer limiting process and can be attributed to the double-layer capacitance in parallel with the charge transfer resistance at the contact interface between electrode and electrolyte solution.[51,52] Figure 10 shows typical EIS Nyquist plots of bare $BiVO_4$, $BiVO_4$–rGO–U, and $BiVO_4$–rGO, revealing major

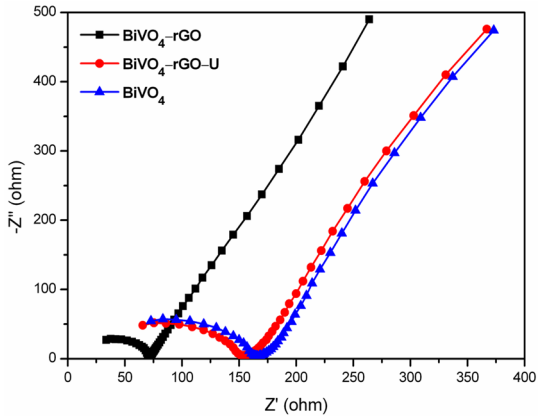

Figure 10. Electrochemical impedance spectroscopy Nyquist plots of bare $BiVO_4$, $BiVO_4$–rGO–U, and $BiVO_4$–rGO nanocomposites.

semicircle arcs and straight lines. Taking the same preparation of electrodes and electrolyte into account, the high frequency semicircles can be attributed to the resistance of the electrodes. As compared to bare $BiVO_4$ and $BiVO_4$–rGO–U, the impedance plot of $BiVO_4$–rGO exhibits an obvious smaller radius, indicating faster interfacial electron transfer. It is thus believed that the strong chemical bonding between $BiVO_4$ and rGO will facilitate the interfacial charge transfer, which is in accordance with its enhanced photoactivity.

To further understand the transfer and recombination processes of photoexcited charge carriers in these samples, PL spectra were measured. PL measurement has been employed to investigate the fate of electron–hole pairs in semiconductor successfully.[53,54] As displayed in Figure 11, the

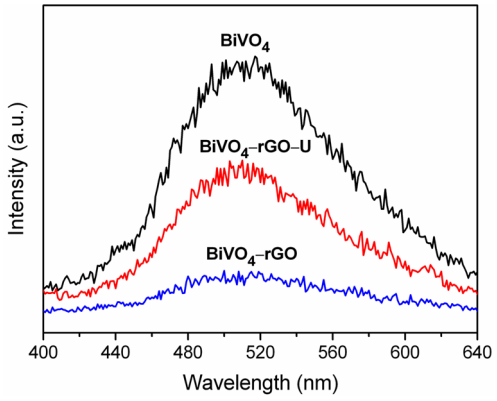

Figure 11. PL spectra of bare $BiVO_4$, $BiVO_4$–rGO–U, and $BiVO_4$–rGO nanocomposites.

emission of as-prepared samples is centered at 520 nm, corresponding to the recombination of holes in the valence band and electrons in conduction band. The PL intensity obtained over $BiVO_4$–rGO is one-third of $BiVO_4$–rGO–U, and one-sixth of bare $BiVO_4$, showing a considerable fluorescence quenching after the introduction of rGO. The fluorescence quenching mainly results from sufficient interfacial contact between $BiVO_4$ particles and rGO nanosheets. Similar phenomena have been previously reported in various nanocomposites.[55–57] In brief, the photogenerated electrons in excited $BiVO_4$ are transferred to rGO nanosheets immediately after the photoproduction, separating the photogenerated electrons and holes and inhibiting their recombination

efficiently. The result is well in accordance with EIS analysis, and the enhancement of photoactivity is sensible.

With the above analyses, the improvement can be illustrated by a reaction mechanism as depicted in Scheme 2. Under visible light irradiation (λ > 400 nm), electrons in the valence band (VB) are excited to the conduction band (CB), leaving holes in VB and generating electron–hole pairs in $BiVO_4$ particles. The photogenerated electrons (e^-) and holes (h^+) then transfer to $BiVO_4$ particle surfaces to react with water and O_2 to produce highly active free radicals ($O_2^{\cdot-}$, $^{\cdot}OH$). These free radicals are able to attack many organics, achieving pollutant photodegradation through photocatalytic redoxreactions.[58] Undoubtedly, separation and transportation of photogenerated charge carriers are crucial factors influencing the photoactivity. In consideration of that, the best photocatalytic activity of $BiVO_4$–rGO powders among the as-prepared samples is merited. From the above discussion, we could assert that surface charge modification provides a rational way in constructing $BiVO_4$–rGO nanocomposite photocatalysts with sufficient interfacial contact and small particle size via electrostatic self-assembly. The synergistic effect between the microscopic crystal structure of $BiVO_4$ and the improved interfacial interaction of $BiVO_4$–rGO composites not only increases photocatalytic reaction sites and photoresponding range, but also promotes the separation efficiency of electron–hole pairs, thus significantly enhancing the photoactivity.

Scheme 2. A Schematic Reaction Mechanism Illustrating the Photocatalytic Redoxreactions over $BiVO_4$–rGO Nanocomposite Photocatalysts under Visible Light Irradiation (λ > 400 nm)

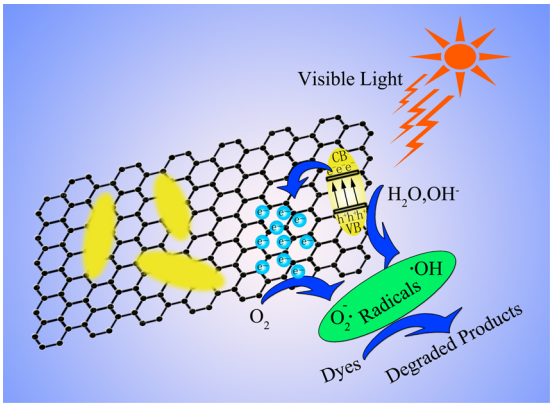

CONCLUSIONS

In summary, $BiVO_4$–rGO nanocomposite photocatalysts with excellent visible light photocatalytic activities have been synthesized by electrostatic self-assembly via a simple surface charge modification on amorphous $BiVO_4$ powders with silane coupling agent. For comparison, $BiVO_4$–rGO–U synthesized without surface charge modification and bare $BiVO_4$ powders have also been prepared. Morphology characterizations reveal that the $BiVO_4$ nanoparticles in the framework of $BiVO_4$–rGO nanocomposite possess much smaller particle size than those in the framework of $BiVO_4$–rGO–U and bare $BiVO_4$. The smaller particle size with high surface areas and increased interfacial interaction in $BiVO_4$–rGO leads to increased photocatalytic reaction sites, extended photoresponding range, and enhanced photogenerated charge separation and transportation efficiency. All of these factors result in enhanced photocatalytic performance. The present work highlights that sufficient interfacial contact between semiconductor and rGO can be obtained by electrostatic self-assembly via surface charge modification on amorphous semiconductor precursors. It is expected that the simple modification strategy could be employed to construct highly active graphene-based nanocomposite photocatalysts for photocatalytic degradation of pollutants and hydrogen generation from water splitting.

ASSOCIATED CONTENT

Supporting Information

Synthesis of GO, XPS, EDS, HRTEM characterization of $BiVO_4$–rGO, and additional photodegradation rates of blank photolysis experiments for MB and RhB. This material is available free of charge via the Internet at http://pubs.acs.org.

AUTHOR INFORMATION

Corresponding Author

*E-mail: binlu@zju.edu.cn.

Notes

The authors declare no competing financial interest.

ACKNOWLEDGMENTS

This work was financially supported by the National Natural Science Foundation of China (Grants 51002134, 11374009, 51302244, 61376094), and the 973 Program (2011CB921903).

REFERENCES

(1) Fujishima, A.; Honda, K. Electrochemical Photolysis of Water at a Semiconductor Electrode. *Nature* **1972**, *238*, 37–38.
(2) Chen, D.; Ye, J. Hierarchical WO_3 Hollow Shells: Dendrite, Sphere, Dumbbell, and Their Photocatalytic Properties. *Adv. Funct. Mater.* **2008**, *18*, 1922–1928.
(3) Etacheri, V.; Roshan, R.; Kumar, V. Mg-Doped ZnO Nanoparticles for Efficient Sunlight-Driven Photocatalysis. *ACS Appl. Mater. Interfaces* **2012**, *4*, 2717–2725.
(4) Jing, D.; Guo, L. A Novel Method for the Preparation of a Highly Stable and Active CdS Photocatalyst with a Special Surface Nanostructure. *J. Phys. Chem. B* **2006**, *110*, 11139–11145.
(5) Bi, Y.; Ouyang, S.; Umezawa, N.; Cao, J.; Ye, J. Facet Effect of Single-Crystalline Ag_3PO_4 Sub-microcrystals on Photocatalytic Properties. *J. Am. Chem. Soc.* **2011**, *133*, 6490–6492.
(6) Nakata, K.; Fujishima, A. TiO_2 Photocatalysis: Design and applications. *J. Photochem. Photobiol., C* **2012**, *13*, 169–189.
(7) Chen, X.; Shen, S.; Guo, L.; Mao, S. S. Semiconductor-based Photocatalytic Hydrogen Generation. *Chem. Rev.* **2010**, *110*, 6503–6570.
(8) Hariharan, C. Photocatalytic Degradation of Organic Contaminants in Water by ZnO Nanoparticles: Revisited. *Appl. Catal., A* **2006**, *304*, 55–61.
(9) An, X.; Yu, J. C.; Wang, Y.; Hu, Y.; Yu, X.; Zhang, G. WO_3 Nanorods/Graphene Nanocomposites for High-efficiency Visible-light-driven Photocatalysis and NO_2 Gas Sensing. *J. Mater. Chem.* **2012**, *22*, 8525–8531.
(10) Zhang, H.; Huang, H.; Ming, H.; Li, H.; Zhang, L.; Liu, Y.; Kang, Z. Carbon Quantum Dots/Ag_3PO_4 Complex Photocatalysts With Enhanced Photocatalytic Activity and Stability under Visible Light. *J. Mater. Chem.* **2012**, *22*, 10501–10506.
(11) Burda, C.; Lou, Y.; Chen, X.; Samia, A. C. S.; Stout, J.; Gole, J. L. Enhanced Nitrogen Doping in TiO_2 Nanoparticles. *Nano Lett.* **2003**, *3*, 1049–1051.
(12) Tong, H.; Ouyang, S.; Bi, Y.; Umezawa, N.; Oshikiri, M.; Ye, J. Nano-photocatalytic Materials: Possibilities and Challenges. *Adv. Mater.* **2012**, *24*, 229–251.

(13) Ni, M.; Leung, M. K. H.; Leung, D. Y. C.; Sumathy, K. A Review and Recent Developments in Photocatalytic Water-splitting Using for Hydrogen Production. *Renewable Sustainable Energy Rev.* **2007**, *11*, 401−425.
(14) Kudo, A.; Miseki, Y. Heterogeneous Photocatalyst Materials for Water Splitting. *Chem. Soc. Rev.* **2009**, *38*, 253−278.
(15) Zhang, H.; Lv, X. J.; Li, Y. M.; Wang, Y.; Li, J. H. P25-Graphene Composite as a High Performance Photocatalyst. *ACS Nano* **2010**, *4*, 380−386.
(16) Liu, X.; Pan, L.; Lv, T.; Zhu, G.; Sun, Z.; Sun, C. Microwave-assisted Synthesis of CdS-reduced Graphene Oxide Composites for Photocatalytic Reduction of Cr(VI). *Chem. Commun.* **2011**, *47*, 11984−11986.
(17) Bu, Y.; Chen, Z.; Li, W.; Hou, B. Highly Efficient Photocatalytic Performance of Graphene−ZnO Quasi-Shell−Core Composite Material. *ACS Appl. Mater. Interfaces* **2013**, *5*, 12361−12368.
(18) Yang, X.; Cui, H.; Li, Y.; Qin, J.; Zhang, R.; Tang, H. Fabrication of Ag_3PO_4-Graphene Composites with Highly Efficient and Stable Visible Light Photocatalytic Performance. *ACS Catal.* **2013**, *3*, 363−369.
(19) Fan, W. Q.; Lai, Q. H.; Zhang, Q. H.; Wang, Y. Nanocomposites of TiO_2 and Reduced Graphene Oxide as Efficient Photocatalysts for Hydrogen Evolution. *J. Phys. Chem. C* **2011**, *115*, 10694−10701.
(20) Williams, G.; Seger, B.; Kamat, P. V. TiO_2-Graphene Nanocomposites. UV-assisted Photocatalytic Reduction of Graphene Oxide. *ACS Nano* **2008**, *2*, 1487−1491.
(21) Liu, Q.; Liu, Z.; Zhang, X.; Yang, L.; Zhang, N.; Pan, G.; Yin, S.; Chen, Y.; Wei, J. Polymer Photovoltaic Cells Based on Solution-processable Graphene and P3HT. *Adv. Funct. Mater.* **2009**, *19*, 894−904.
(22) Su, C.; Acik, M.; Takai, K.; Lu, J.; Hao, S.-j.; Zheng, Y.; Wu, P.; Bao, Q.; Enoki, T.; Chabal, Y. J.; Loh, K. P. Probing the Catalytic Activity of Porous Graphene Oxide and the Origin of This Behaviour. *Nat. Commun.* **2012**, *3*, 1298−1316.
(23) Kudo, A.; Ueda, K.; Kato, H.; Mikami, I. Photocatalytic O_2 Evolution Under Visible Light Irradiation on $BiVO_4$ in Aqueous $AgNO_3$ Solution. *Catal. Lett.* **1998**, *53*, 229−230.
(24) Park, Y.; McDonald, K. J.; Choi, K. S. Progress in Bismuth Vanadate Photoanodes for Use in Solar Water Oxidation. *Chem. Soc. Rev.* **2013**, *42*, 2321−2337.
(25) Tan, G. Q.; Zhang, L. L.; Ren, H. J.; Wei, S. S.; Huang, J.; Xia, A. Effects of pH on the Hierarchical Structures and Photocatalytic Performance of $BiVO_4$ Powders Prepared via the Microwave Hydrothermal Method. *ACS Appl. Mater. Interfaces* **2013**, *5*, 5186−5193.
(26) Nguyen, T.; Le, T.; Truong, D.; Fehrmann, R.; Riisager, A.; Van Driessche, I. Synergy Effects in Mixed Bi_2O_3, MoO_3 and V_2O_5 Catalysts for Selective Oxidation of Propylene. *Res. Chem. Intermed.* **2012**, *38*, 829−846.
(27) Jiang, H.; Dai, H.; Meng, X.; Ji, K.; Zhang, L.; Deng, J. Porous olive-like $BiVO_4$: Alcoho-hydrothermal Preparation and Excellent Visible-light-driven Photocatalytic Performance for the Degradation of Phenol. *Appl. Catal., B* **2011**, *105*, 326−334.
(28) Zhao, Z.; Li, Z.; Zou, Z. Electronic Structure and Optical Properties of Monoclinic Clinobisvanite $BiVO_4$. *Phys. Chem. Chem. Phys.* **2011**, *13*, 4746−4753.
(29) Xi, G.; Ye, J. Synthesis of Bismuth Vanadate Nanoplates with Exposed {001} Facets and Enhanced Visible-light Photocatalytic Properties. *Chem. Commun.* **2010**, *46*, 1893−1895.
(30) Martínez-de la Cruz, A.; García-Pérez, U. M.; Sepúlveda-Guzmán, S. Characterization of the Visible-light-driven $BiVO_4$ Photocatalyst Synthesized via a Polymer-assisted Hydrothermal Method. *Res. Chem. Intermed.* **2013**, *39*, 881−894.
(31) Eda, S.-i.; Fujishima, M.; Tada, H. Low Temperature-synthesis of $BiVO_4$ Nanorods Using Polyethylene Glycol as a Soft Template and the Visible-light-activity for Copper Acetylacetonate Decomposition. *Appl. Catal., B* **2012**, *125*, 288−293.
(32) Yu, J. Q.; Kudo, A. Hydrothermal Synthesis of Nanofibrous Bismuth Vanadate. *Chem. Lett.* **2005**, *34*, 850−851.
(33) Sun, Y.; Wu, C.; Long, R.; Cui, Y.; Zhang, S.; Xie, Y. Synthetic Loosely Packed Monoclinic $BiVO_4$ Nanoellipsoids with Novel Multiresponses to Visible Light, Trace Gas and Temperature. *Chem. Commun.* **2009**, *30*, 4542−4544.
(34) Yan, Y.; Sun, S. F.; Song, Y.; Yan, X.; Guan, W. S.; Liu, X. L.; Shi, W. D. Microwave-assisted in situ Synthesis of Reduced Graphene Oxide-$BiVO_4$ Composite Photocatalysts and Their Enhanced Photocatalytic Performance for the Degradation of Ciprofloxacin. *J. Hazard. Mater.* **2013**, *250*, 106−114.
(35) Yun Hau, N.; Iwase, A.; Bell, N. J.; Kudo, A.; Amal, R. Semiconductor/Reduced Graphene Oxide Nanocomposites Derived From Photocatalytic Reactions. *Catal. Today* **2011**, *164*, 353−357.
(36) Sun, Y.; Qu, B.; Liu, Q.; Gao, S.; Yan, Z.; Yan, W.; Pan, B.; Wei, S.; Xie, Y. Highly Efficient Visible-light-driven Photocatalytic Activities in Synthetic Ordered Monoclinic $BiVO_4$ Quantum Tubes-Graphene Nanocomposites. *Nanoscale* **2012**, *4*, 3761−3767.
(37) Yang, M. Q.; Weng, B.; Xu, Y. J. Improving the Visible Light Photoactivity of In_2S_3-Graphene Nanocomposite via a Simple Surface Charge Modification Approach. *Langmuir* **2013**, *29*, 10549−10558.
(38) Hummers, W. S.; Hummers; Offeman, R. E. Preparation of Graphitic Oxide. *J. Am. Chem. Soc.* **1958**, *80*, 1339−1339.
(39) Lee, C.; Sung, Y. W.; Park, J. W. Multiple Equilibria of Phenothiazine Dyes in Aqueous Cyclodextrin Solutions. *J. Phys. Chem. B* **1999**, *103*, 893−898.
(40) Lai, Y.; Meng, M.; Yu, Y. One-step Synthesis, Characterizations and Mechanistic Study of Nanosheets-constructed Fluffy ZnO and Ag/ZnO Spheres Used for Rhodamine B Photodegradation. *Appl. Catal., B* **2010**, *100*, 491−501.
(41) Zhang, A. P.; Zhang, J. Z.; Cui, N. Y.; Tie, X. Y.; An, Y. W.; Li, L. J. Effects of pH on Hydrothermal Synthesis and Characterization of Visible-light-driven $BiVO_4$ Photocatalyst. *J. Mol. Catal. A: Chem.* **2009**, *304*, 28−32.
(42) Krishnamoorthy, K.; Veerapandian, M.; Mohan, R.; Kim, S.-J. Investigation of Raman and Photoluminescence Studies of Reduced Graphene Oxide Sheets. *Appl. Phys. A: Mater. Sci. Process.* **2012**, *106*, 501−506.
(43) Stankovich, S.; Dikin, D. A.; Piner, R. D.; Kohlhaas, K. A.; Kleinhammes, A.; Jia, Y.; Wu, Y.; Nguyen, S. T.; Ruoff, R. S. Synthesis of Graphene-based Nanosheets via Chemical Reduction of Exfoliated Graphite Oxide. *Carbon* **2007**, *45*, 1558−1565.
(44) Bagwe, R. P.; Hilliard, L. R.; Tan, W. Surface Modification of Silica Nanoparticles to Reduce Aggregation and Nonspecific Binding. *Langmuir* **2006**, *22*, 4357−4362.
(45) Zhu, J. Y.; He, J. H. Facile Synthesis of Graphene-Wrapped Honeycomb MnO_2 Nanospheres and Their Application in Supercapacitors. *ACS Appl. Mater. Interfaces* **2012**, *4*, 1770−1776.
(46) Lee, J. S.; You, K. H.; Park, C. B. Highly Photoactive, Low Bandgap TiO_2 Nanoparticles Wrapped by Graphene. *Adv. Mater.* **2012**, *24*, 1084−1088.
(47) Kumar, K. V.; Porkodi, K.; Rocha, F. Langmuir−Hinshelwood kinetics − A theoretical study. *Catal. Commun.* **2008**, *9*, 82−84.
(48) Fu, H.; Zhang, L.; Yao, W.; Zhu, Y. Photocatalytic Properties of Nanosized Bi_2WO_6 Catalysts Synthesized via a Hydrothermal Process. *Appl. Catal., B* **2006**, *66*, 100−110.
(49) Butler, M. A. Photoelectrolysis and Physical Properties of the Semiconducting Electrode WO_2. *J. Appl. Phys.* **1977**, *48*, 1914−1920.
(50) Gao, E.; Wang, W.; Shang, M.; Xu, J. Synthesis and Enhanced Photocatalytic Performance of Graphene-Bi_2WO_6 Composite. *Phys. Chem. Chem. Phys.* **2011**, *13*, 2887−2893.
(51) Zhang, N.; Zhang, Y.; Pan, X.; Fu, X.; Liu, S.; Xu, Y.-J. Assembly of CdS Nanoparticles on the Two-Dimensional Graphene Scaffold as Visible-Light-Driven Photocatalyst for Selective Organic Transformation under Ambient Conditions. *J. Phys. Chem. C* **2011**, *115*, 23501−23511.
(52) Lu, T.; Zhang, Y.; Li, H.; Pan, L.; Li, Y.; Sun, Z. Electrochemical Behaviors of Graphene−ZnO and Graphene−SnO_2 Composite Films for Supercapacitors. *Electrochim. Acta* **2010**, *55*, 4170−4173.
(53) Eda, G.; Lin, Y.-Y.; Mattevi, C.; Yamaguchi, H.; Chen, H.-A.; Chen, I. S.; Chen, C.-W.; Chhowalla, M. Blue Photoluminescence

from Chemically Derived Graphene Oxide. *Adv. Mater.* **2010**, *22*, 505−509.
(54) Tang, J.; Zou, Z.; Ye, J. Photophysical and Photocatalytic Properties of $AgInW_2O_8$. *J. Phys. Chem. B* **2003**, *107*, 14265−14269.
(55) Zhou, K.; Zhu, Y.; Yang, X.; Jiang, X.; Li, C. Preparation of Graphene-TiO_2 Composites with Enhanced Photocatalytic Activity. *New J. Chem.* **2011**, *35*, 353−359.
(56) Williams, G.; Kamat, P. V. Graphene−Semiconductor Nanocomposites: Excited-State Interactions between ZnO Nanoparticles and Graphene Oxide. *Langmuir* **2009**, *25*, 13869−13873.
(57) Gao, Z.; Liu, N.; Wu, D.; Tao, W.; Xu, F.; Jiang, K. Graphene−CdS Composite, Synthesis and Enhanced Photocatalytic Activity. *Appl. Surf. Sci.* **2012**, *258*, 2473−2478.
(58) Chen, C.; Ma, W.; Zhao, J. Semiconductor-mediated Photodegradation of Pollutants Under Visible-light Irradiation. *Chem. Soc. Rev.* **2010**, *39*, 4206−4219.